Nano Energy 43 (2018) 317–325

Contents lists available at ScienceDirect

Nano Energy

journal homepage: www.elsevier.com/locate/nanoen

Full paper

Atomic layer deposition-enabled ultrastable freestanding carbon-selenium cathodes with high mass loading for sodium-selenium battery

Dingtao Ma[a,c,d,1], Yongliang Li[a,1], Jingbo Yang[a], Hongwei Mi[a], Shan Luo[a], Libo Deng[a], Chaoyi Yan[a], Peixin Zhang[a,*], Zhiqun Lin[b,*], Xiangzhong Ren[a], Jianqing Li[c], Han Zhang[d]

[a] College of Chemistry and Environmental Engineering, Shenzhen University, Shenzhen 518060, China
[b] School of Materials Science and Engineering, Georgia Institute of Technology, Atlanta, GA 30332, USA
[c] Faculty of Information Technology, Macau University of Science and Technology, Macau 519020, China
[d] SZU-NUS Collaborative Innovation Center for Optoelectronic Science and Technology and Key Laboratory of Optoelectronic Devices and Systems of Ministry of Education and Guangdong Province, Shenzhen University, Shenzhen 518060, China

ARTICLE INFO

Keywords:
Sodium ion batteries
Atomic layer deposition
Carbon-selenium cathode
High mass loading
Energy storage

ABSTRACT

Melt diffusion followed by vapor deposition is judiciously combined with atomic layer deposition (ALD) to construct Al_2O_3–coated (Se/porous N-doped carbon nanofibers)@Se composite (denoted SC@Se-Al_2O_3) materials for sodium-selenium (Na-Se) batteries. High mass loading, ultrastable and free-standing carbon-selenium cathode is conveniently achieved by tailoring both the Se content and the thickness of deposited Al_2O_3 layer. Importantly, in contrast to only 176 mAh g^{-1} of the electrode without Al_2O_3 deposition after 660 cycles, the composite with a Se content of 67 wt% and a 3-nm Al_2O_3 thickness retains a reversible capacity of 503 mAh g^{-1} after 1000 cycles with no capacity fading at 0.5 A g^{-1}. These findings clearly suggest that ALD strategy provides a viable, controllable and effective means of tuning the electrode performance towards high mass loading of active materials and long cycle life of the resulting battery for energy storage applications.

1. Introduction

Sodium-selenium (Na-Se) batteries has recently received much attention for large-scale energy-storage applications as they possess high energy density and excellent safety and cyclic stability. They carry several advantageous attributes including low cost and wide availability of sodium resources [1–6], as well as their moderate theoretical gravimetric capacity (678 mA h g^{-1}) and high volumetric capacity of Se (~3270 mAh cm^{-3}). However, the polyselenide dissolution, poor electronic conductivity and inferior cycling stability are the challenges that plague the development of Na-Se batteries [7–12].

High specific energy densities are greatly desirable for developing practical energy storage devices. Therefore, the ability to construct cathodes with high Se loading is recognized as one of the essential steps towards building Na-Se batteries with optimized performance. However, the Se contents in the reported cathode composites are relatively low (30–54 wt%) [10–14], leading to a reduced specific energy density of the resulting Na-Se batteries. Moreover, additives such as carbon black and polymer binders are usually required to improve the mechanical integrity and electronic conductivity of electrodes, which result in a further reduction in volumetric energy densities. Na-Se batteries with excellent mechanical flexibility, high specific energy density and excellent cyclic stability are highly beneficial for potential applications in wearable energy storage devices.

In this context, to achieve Na-Se batteries with long-term stability, strong chemical binding is required in order to prevent the dissolution of sodium polyselenides into electrolyte. Porous carbon can act as a conductive framework to entrap selenium, which promotes the reduction of polyselenide dissolution and improves the electronic conductivity of selenium [15–19]. The electronic and chemical properties of carbon framework can also be modulated by the introduction of heteroatoms via structure modification [20]. Moreover, it is important to note that metal oxides particles, such as Al_2O_3 [21,22], TiO_2 [23] and SiO_2 [24], have been found to act as effective adsorbents for tethering the soluble polysulfides. However, such modifications are usually achieved by wet chemistry approaches, making it difficult to control the particle size and thus leading to incompact interfacial contacts between the components in batteries. Atomic layer deposition (ALD) technique has been widely employed in various fields including lithium ion batteries (LIBs) and SIBs [25–27], to render uniform thin film deposition

* Corresponding authors.
E-mail addresses: pxzhang@szu.edu.cn (P. Zhang), zhiqun.lin@mse.gatech.edu (Z. Lin).
[1] These authors contributed equally to this work and should be considered as co-first authors.

https://doi.org/10.1016/j.nanoen.2017.11.042
Received 17 August 2017; Received in revised form 6 October 2017; Accepted 17 November 2017
Available online 21 November 2017

on arbitrary surfaces.

Herein, we report on the judicious crafting of ALD-deposited, ultrastable and freestanding carbon-Se cathodes with high Se loading for Na-Se batteries. First, flexible and porous carbon nanofiber mats are produced by electrospinning and utilized as conductive matrix. Subsequently, high Se loading with tunable content up to 70 wt% is achieved by two consecutive Se infiltrations (i.e., melt diffusion and vapor deposition). A number of Al_2O_3 layers are then deposited on the porous composite electrodes by ALD for effective prevention of polyselenide dissolution. Intriguingly, the Al_2O_3 deposition leads to a negligible weight increase while the stability of electrode is significantly improved. It is worth noting that this is the first report of ALD-enabled Se-based cathode materials for Na-Se batteries. The effect of the Al_2O_3 thickness deposited by ALD on the electrochemical performances of Na-Se batteries is systematically studied. Particularly, the electrode with 67 wt% of Se content and 25 Al_2O_3 layers exhibits an outstanding cyclic stability and electrochemical performance, and delivers an impressive specific capacity of 503.5 mAh g^{-1} after 1000 cycles at 0.5 A g^{-1} with a capacity retention of 71.2%. This is in sharp contrast to the 23.1% retention of the bare electrode (i.e., without ALD coating of Al_2O_3) after 660 cycles, demonstrating its promising potential as an advanced cathode for Na-Se batteries.

2. Experimental

2.1. Preparation of the porous N-doped carbon nanofibers

The porous N-doped carbon nanofibers (PCNFs) were synthesized by using electrospinning technique combined with the carbonization process. (1) Typically, 1.4 g polyacrylonitrile (PAN) and 0.05 g F127 were dissolved into 15 mL dimethylformamide (DMF) organic solvent and stirred for at least 12 h to form a clear solution as the spinning solution. Then, the as-prepared solution was loaded into a 25 mL syringe pump, and the electrospinning process was conducted under 14.5 kV applied voltage and 1.5 mL h^{-1} feeding rate, as well as 15 cm collected distance. Finally, non-woven film can be easily peeled off from the collector and successively dried at 80 °C under vacuum for 8 h. (2) Dried film was stabilized at 280 °C for 4 h in air and then carbonized at 850 °C for another 6 h at 2 °C min^{-1} heating rate under N_2 atmosphere.

2.2. Preparation of the (Se/PCNFs)@Se composite

The PCNFs were punched to disc with a 0.6 cm radius and mixed with Se powder. Subsequently, they were heated to 260 °C for 12 h and then 300 °C for 3 h in an Ar-filled tubular furnace to yield the Se/PCNFs (denoted SC) composite. After that, the SC composite and additional Se powder were respectively loaded in two sides of an alumina boat with a sealed cover and placed in a quartz tube reactor again, which was heated at 350 °C for 2 h under flowing Ar gas, yielding (Se/PCNFs)@Se composite (denoted SC@Se).

2.3. Preparation of the Al_2O_3–coated SC@Se composites by ALD

The Al_2O_3 protective layer was directly grown on the freestanding SC@Se electrode using KE-MICRO PEALD-200A machine under 4×10^{-3} Torr at 150 °C. Typically, trimethylaluminum (TMA, Fornano, 99.9999%) and deionized H_2O were used as the aluminum and oxygen source, respectively. Ar (99.999%) gas was used as the carrier gas with a flow rate of 20 sccm. Typically, a complete atomic layer deposition (ALD) cycle consisting of a sequential and alternating supply of TMA and H_2O as follows: a 0.05 s supply of TMA vapor, a 7 s exposure of TMA to the electrodes, a 60 s-Ar purge, a 0.06 s supply of water vapor, a 7 s extended exposure of H_2O to the electrodes, and 70 s-Ar purge. The ALD process were conducted for 0, 10, 25, 40 cycles to produce a series of the Al_2O_3–coated SC@Se composites (denoted SC@Se-xAl_2O_3 composites; where x = 0, 10, 25, and 40 cycles). It is notable that the content of Al_2O_3 was difficult to be accurately measured in the composite due to its ultrasmall amount.

2.4. Physical characterizations

The morphology and microstructure of SC@Se-xAl_2O_3 composites were examined by FESEM (JSM-7800F & TEAM Octane Plus) and HRTEM (Tecnai G2 F30). The structure and Raman spectrum were collected on X-ray diffraction (Bruker, D8 Advance with Cu-Ka radiation) and Raman microscope (DXR Thermo-Fisher Scientific), respectively. Thermogravimetric analysis (TGA-Q50) was performed under nitrogen atmosphere from room temperature up to 700 °C with a heating rate of 10 °C min^{-1}. BELSORP-max Surface Area and Porosimetry instrument was used to measure the nitrogen adsorption/desorption isotherms of electrodes. X-ray photoelectron spectroscopy (XPS) tests were carried out using an ESCALAB 250Xi system, and all data were calibrated using adventitious C1s peak at a fixed value of 284.4 eV. To prepare HRTEM samples, a trace amount of samples were added into ethanol solution with ultrasonic dispersion for 1 h, and then dropped to the micro Cu grid and dried.

2.5. Electrochemical measurements

The electrochemical tests were performed with CR2032 coin-type cells, which were assembled with sodium metal as the counter and reference electrodes inside an argon-filled glove box (MBRAUN, UNILab2000, both moisture and oxygen levels below 1 ppm). Glass fiber (Whatman) was used as the separator. The electrolyte was 1 M of $NaClO_4$ in a mixture of ethylene carbonate (EC) and diethyl carbonate (DEC) (1:1 v/v). The freestanding SC@Se-xAl_2O_3 composites were directly used as the working electrodes without any other binders and carbon conductors. The loading mass of the active material was 1.2–1.6 mg cm^{-2}. The galvanostatic charge-discharge tests were carried out over a voltage range of 1.0–3.0 V (vs. Na^+/Na) on a battery test system (Land, CT-2001A) (1 C = 675 mA g^{-1}). Electrochemical impedance spectroscopy (EIS) measurements were performed using the electrochemical workstation (CHI760D) by applying a voltage of 5 mV over a frequency of 10^{-2}-10^5 Hz. All the cells were held at ambient temperature for at least 8 h before tests. All the specific capacity in this study was calculated on the basis of the selenium mass loading. For the ex-situ SEM tests, all procedures were performed in a glove box filled with argon, and tested electrodes were carefully washed with DEC solvent for three times and dried.

3. Results and discussion

Fig. 1a illustrates the step-wise preparation procedure for SC@Se-xAl_2O_3 composites. Notably, the intensive chemical activation was found to cause a large specific surface area that renders a high Se loading. However, it also led to a poor conductivity and a low mechanical strength of the carbon matrix [9–12]. To address this unfavorable issue, the freestanding porous PCNFs were produced by electrospinning, followed by the carbonization process without further chemical activation (1st panel in Fig. 1a; see Section 2). The SC composites were first formed via a simple melt-diffusion of elemental Se (2nd panel in Fig. 1a). Specifically, the solid Se powder tended to melt and diffuse into the mesoporous carbon matrix during this process. The successful diffusion was substantiated as discussed later. The composites were then further treated with the different mass ratio of Se powder by vapor deposition to create the SC@Se composites (3rd panel in Fig. 1a). Finally, the Al_2O_3 protective layers with nanometer thickness were directly deposited onto the SC@Se composites using ALD process, where a number of ALD cycles were applied to yield the Al_2O_3 coating with varied thickness (4th panel in Fig. 1a).

The PCNFs clearly exhibit a continuous and interconnected

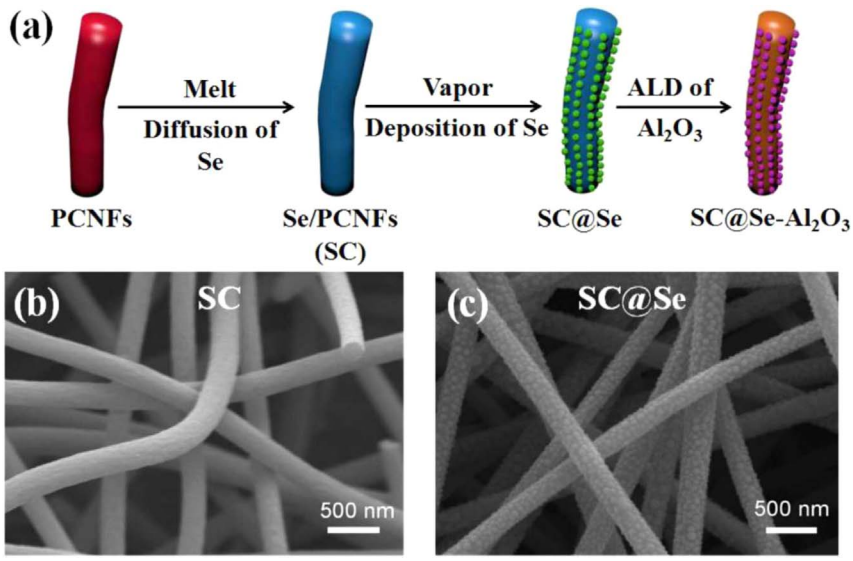

Fig. 1. (a) Schematic illustration of the preparation process for SC@Se-xAl_2O_3 composites. FESEM images of (b) SC and (c) SC@Se composites.

structure with an average nanofiber diameter of 200 nm (Fig. S1). Upon heating the mixture containing Se powder and PCNFs, Se was diffused into PCNFs to form the SC composites as shown in Fig. 1b (see Section 2). No Se residues were found on the surface of the composite. The corresponding elemental mapping (Fig. S2) and EELS mappings (Fig. S3) also suggested the uniform distribution of Se element inside the PCNFs. To further improve the Se mass loading due to its possible limited impregnation within PCNFs and prevent the structural damage of the carbon matrix of PCNFs, the Se vapor deposition was carefully conducted to yield SC@Se composites. Interestingly, Fig. 1c clearly shows Se nanoparticles grown on the surface of SC composites with an average size of a few tens of nanometers. By tuning the mass ratio of SC to the Se powder, different Se content of SC@Se composites can be obtained (Fig. S4).

The ALD deposition of Al_2O_3 on SC@Se was then performed to yield the SC@Se-xAl_2O_3 composites. The Al_2O_3 coating functions as effective adsorbent for preventing polyselenide dissolution. It is notable that for the SC@Se-xAl_2O_3 (x = 10, 25 and 40 layers) composites, no obvious morphology changes were observed after the ALD process as compared to SC@Se (Fig. S5). The mechanical properties of both SC@Se and SC@Se-xAl_2O_3 composites were evaluated by nanoindentation measurements (Fig. S6). The results showed that the Al_2O_3 coating created by ALD can enhance the Young's modulus and the hardness of freestanding electrodes with the increase of deposition layers. Besides, the obtained freestanding electrodes showed a good flexibility where 180° bending and 360° twisting did not lead to any structural damages (Fig. S7a). To demonstrate its potential for flexible electronics application, the flake-type Na-Se battery was assembled to power a commercial LED (Figs. S7b–d). Quite intriguingly, the yellow LED can be easily lighted up even when the battery was bent to 180°, signifying its promising potential for flexible energy storage devices.

Microstructure of SC@Se-xAl_2O_3 composites were characterized by HRTEM and EELS elemental mapping in Fig. 2. The central was amorphous Se layer (the inset SAED images in Fig. 2c and e) with a thickness of approximately 20–30 nm on the surface of the carbon matrix was tightly wrapped by Al_2O_3 layers (Fig. S8). The thickness of the outer Al_2O_3 layers can be precisely controlled by adjusting the ALD cycle number. Fig. 2(a, c, e) show the Al_2O_3 layer thickness of 1.5, 3 and 5 nm produced from the deposition cycles of 10, 25 and 40, respectively. The growing rate was calculated to be 0.12 nm per cycle (Fig. S9). The EELS mapping of the SC@Se-xAl_2O_3 composites are shown in Fig. 2b, d and f. For all the composites, the most intense Al and O signals were found to be near the edges of the imaged area, where the signal was mainly originated from the Al_2O_3 shell. In contrast, the strongest C and Se signals were seen in the center of nanofiber. These results clearly suggested a core-shell structure of composites [28–30]. Besides, the corresponding EDS analysis (Fig. S10) also suggested the uniform elemental distribution of C, N, Se, O and Al within the SC@Se-xAl_2O_3 composites.

In order to understand the compositional change of samples before and after the Se impregnation process and the subsequent ALD deposition, XRD measurements were conducted. Fig. 3a shows the XRD patterns of PCNFs and SC@Se-xAl_2O_3 composites where x = 0, 10, 25 and 40 layers. The characteristic peaks of Se were not observed in the SC@Se-xAl_2O_3 composites after the melt diffusion (1st panel in Fig. 1a) and vapor deposition (2nd panel in Fig. 1a), indicating a highly dispersed, amorphous and short-chain state of Se_n within and onto PCNFs [14,16]. Moreover, no characteristic peaks of Al_2O_3 layers were detected as well due to their trace amount. The weight percentage of Se in the SC@Se composites can be estimated by TG analysis. Fig. 3b compares the TG curves of pristine PCNFs, SC, and SC@Se (SC:Se = 1:0.6; mass ratio) composites measured under nitrogen atmosphere at a heating rate of 10 °C min^{-1}. A mild weight loss (~6 wt%) from 80 °C to 700 °C for PCNFs was seen due to the evaporation of adsorbed water and gradual decomposition of oxygen-containing groups in PCNFs. Thus, the Se content in SC (~59 wt%) and SC@Se (~67 wt%) composites can be estimated by subtracting the weight loss of PCNFs. It is noted that the Se content of SC@Se composites can be readily tuned from 62 wt% to 70 wt% by adjusting the mass ratio of SC and Se powder in the Se vapor deposition process (Fig. S11).

The nitrogen adsorption-desorption isotherms of PCNFs can be identified as type IV isotherm with a relative pressure of around 0.5, which is a typical adsorption behavior of mesoporous materials (Fig. 3c). The pore size distribution showed that the majority of pore size is in a range of 2–12 nm determined by the Barrett-Joyner-Halenda (BJH) analysis. However, accompanied by the disappearance of mesoporous pore within PCNFs, the specific surface area decreased from 584 $m^2 g^{-1}$ (for PCNFs) to 23 $m^2 g^{-1}$(for SC) and 18 $m^2 g^{-1}$ (for SC@Se) after the Se impregnation, indicating the successful loading of Se into the inner pores of PCNFs.

Fig. 3d compares the characteristic Raman peaks of Se, PCNFs, and the SC@Se composites. Both PCNFs and the SC@Se composites exhibited similar peaks located at 1340 and 1570 cm^{-1}, which can be assigned to the D-band of disordered sp^3 and G-band of graphitic sp^2 stretching. It is clear that the Se impregnation and Al_2O_3 coating do not influence the I_D/I_G ratio (Fig. S12). Pristine Se displayed three characteristic peaks of Se-Se bonding vibration located at 140, 240 and 457 cm^{-1}. For SC@Se-xAl_2O_3 (x = 10, 25 and 40 layers) composites,

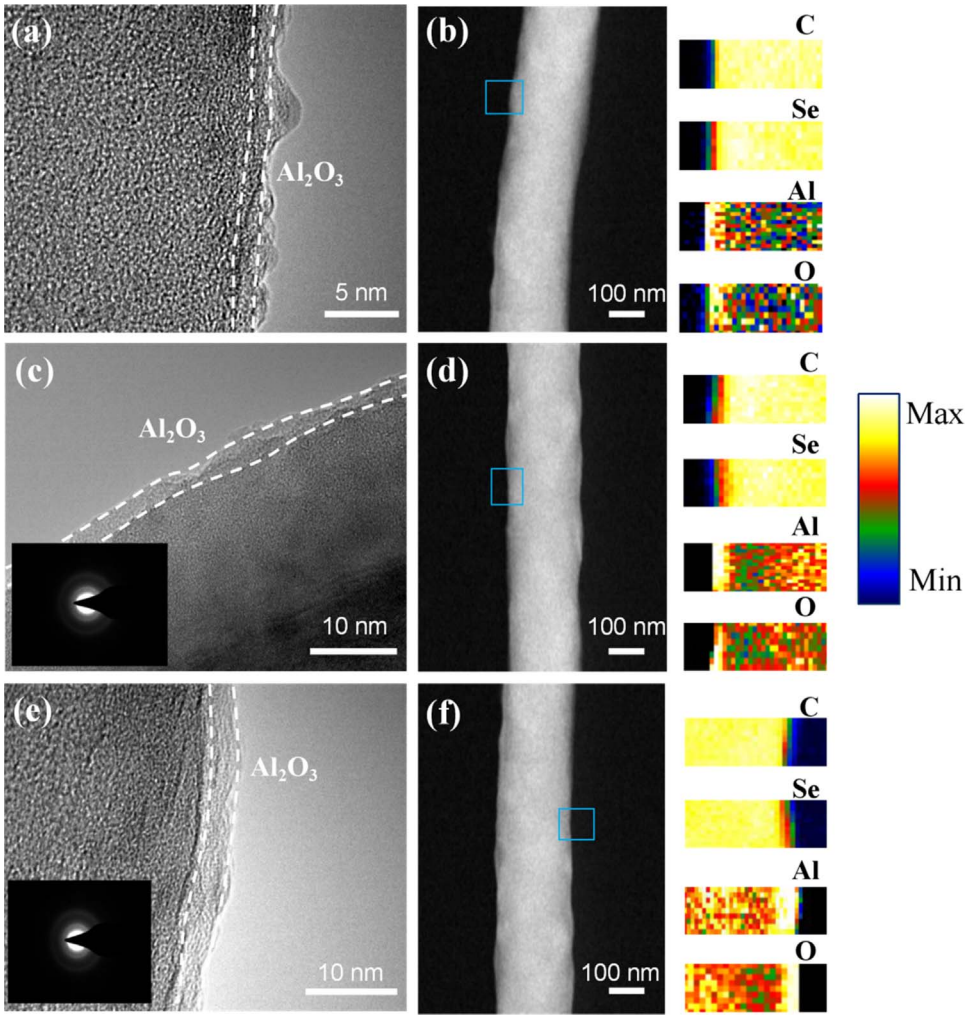

Fig. 2. HRTEM images and high angle annular dark field (HAADF) micrographs with electron energy loss spectroscopy (EELS) elemental mapping of C, Se, Al and C of the SC@Se-xAl_2O_3 composites, obtained after different x cycles of Al_2O_3 deposition by ALD to increase the mechanical stability of composites, where (a, b) for x = 10, (c, d) for x = 25 and (e, f) for x = 40 cycles, respectively.

they all exhibited the Se-Se group vibrations located at 140 and 240 cm^{-1}, as well as the -C-Se- group vibrations located at 290 cm^{-1}. The lower intensity of Se-Se peaks after the ALD process indicates the different atomic configurations of PCNFs after reacting with Se (Fig. S12).

XPS spectra of Se 3d in the SC@Se-xAl_2O_3 composites and pristine Se powder was depicted in Fig. 4a. For the pristine Se, two fitted peaks located at 55.1 and 55.8 eV can be assigned to Se $3d_{5/2}$ and Se $3d_{3/2}$, respectively, based on the spin-orbit coupling [4–6,14]. Clearly, both Se $3d_{5/2}$ and Se $3d_{3/2}$ peaks shifted to higher binding energy after the second Se coating (by vapor deposition; 3rd panel in Fig. 1a) and Al_2O_3 deposition (4th panel in Fig. 1a). Such observation reveals the formation of chemical bonds between Se and other atoms [15,17,19]. Taken together, both Raman and XPS studies demonstrated the existence of Se-C bond in SC@Se-xAl_2O_3 composites, suggesting the close interaction between Se and PCNFs, thus effectively alleviating the volume expansion and improving the electronic conductivity during charge-discharge processes. The comparison of Al 2p XPS spectra for SC@Se-xAl_2O_3 composites at different x were also conducted (Fig. 4b). Obviously, the intensity of Al 2p peak was gradually increased with the increased cycles of Al_2O_3 deposition, implying the formation of thicker layer. Moreover, the deconvolution of N signals of PCNFs is shown in Fig. 4c. Three main peaks located at the binding energies of 398.1, 400.0 and 400.9 eV can be attributed to pyridinic-, pyrrolic- and quaternary-N, respectively, indicating the N-doping in PCNFs, which can enhance the electronic conductivity of PCNFs [31–33]. The weight content of nitrogen in PCNFs was calculated to be 4.67 wt% according to the XPS elemental analysis.

The CR2032 coin-type cells were assembled using SC@Se electrodes with sodium metal as the counter and reference electrodes (see Section 2). The cycling performance of SC@Se electrodes with different Se contents were performed (Fig. S13). Fig. 5a shows the cycling performance of SC@Se-xAl_2O_3 (x = 0, 10, 25 and 40) composites at 0.05 A g^{-1}. The discharge capacities of the first two cycles were 915 and 545 mA h g^{-1} for SC@Se, 890 and 578 mAh g^{-1} for SC@Se-10Al_2O_3, 860 and 589 mA h g^{-1} for SC@Se-25Al_2O_3 and 846 and 478 mAh g^{-1} for SC@Se-40Al_2O_3, respectively. The corresponding capacity retentions were 59.6%, 65%, 68.5% and 56.5%, respectively. Such low retention can partially be ascribed to the irreversible formation of solid electrolyte interface (SEI) film in the first discharge process and the low initial capacity retention (57.3%) of the PCNFs electrode (Fig. S14). In addition, this result also suggested that appropriate thickness (e.g., 25 layers) of the Al_2O_3 layer can effectively improve the capacity efficiency as it promotes the formation of a stable SEI film on the surface of electrode. It is also worth noting that all the electrodes exhibited obvious activation processes with gradually increasing capacity in the first several cycles. The 140th discharge capacities are 461, 491, 548 and 423 mAh g^{-1} for SC@Se, SC@Se-10Al_2O_3, SC@Se-25Al_2O_3 and SC@Se-40Al_2O_3, respectively. The SC@Se-25Al_2O_3 composites displayed the highest capacity retention of 93% with very low capacity fading rate of 0.05% per cycle, signifying a high reversibility of the electrode.

The rate capability of the bare SC@Se and Al_2O_3-coated SC@Se composites was performed and the results are shown in Fig. 5b. It is clear that the SC@Se-25 Al_2O_3 electrode exhibited the best rate

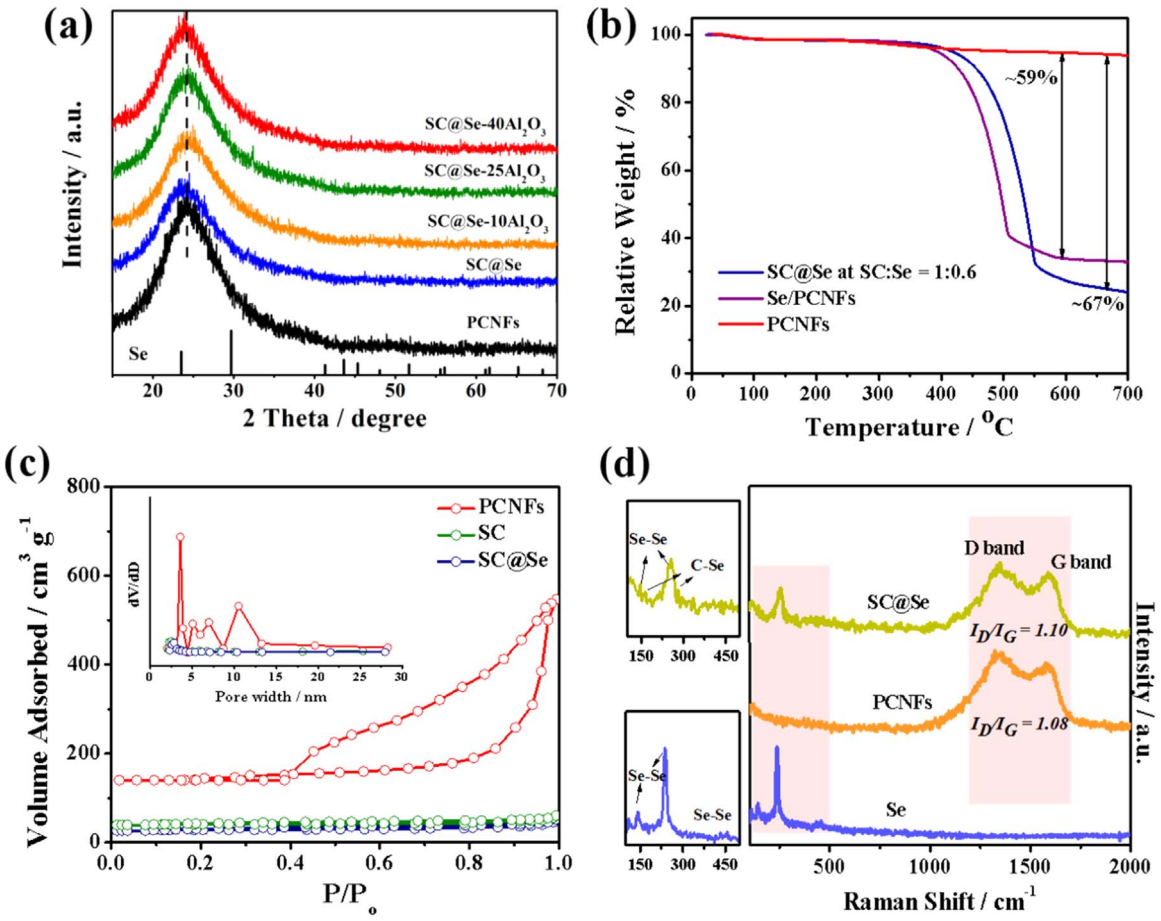

Fig. 3. (a) XRD patterns of Se, PCNFs, and SC@Se-xAl_2O_3 composites (x = 10, 25, and 40). (b) Representative TG analysis of pristine PCNFs, SC, and SC@Se. (c) N_2 adsorption-desorption isotherms and the corresponding pore size distribution of PCNFs, SC and SC@Se (inset), suggesting the presence of micro- and mesopores. (d) Raman spectra of Se, PCNFs, and SC@Se composites.

performance when compared with the bare electrode and other two coated electrodes. Specifically, there was a small difference between the bare SC@Se and the three coated electrodes up to 0.5 C. However, clear differences emerged with the increased rate, especially at 3, 4, 5 and 10 C. Remarkably, the SC@Se-25 Al_2O_3 electrode can retain 69.4%, 53.8%, 45.4% and 27.5% of its initial capacity at 3, 4, 5 and 10 C, respectively, demonstrating higher electrochemical performance than both bare and other coated electrodes. Notably, the capacity retention of SC@Se-40Al_2O_3 electrode dropped below 10% when the current rate increased to 5 and 10 C. This is not surprising as the thick electrochemically inactive and insulating Al_2O_3 film deposited by ALD likely led to much reduced electronic conductivity and ionic diffusion, and thus large polarization and capacity loss [32–35]. For the thinnest coated electrode, a 1.5-nm thick Al_2O_3 protective layer was not thick enough to afford a robust electrode nanostructure during cycling. In the case of SC@Se-25Al_2O_3, a balance between the needed strong binding of polyselenides to Al_2O_3 that prevents it from dissolving in the electrolyte and the decreased electronic and ionic conductivities was reached.

Galvanostatic charge-discharge processes of the SC@Se and SC@Se-25Al_2O_3 electrodes at various rates were evaluated (Fig. S15a and b, respectively). One distinct plateau was observed in each discharge and charge process, corresponding to the reversible reaction between Se and Na. In contrast to the SC@Se electrode, the SC@Se-Al_2O_3 electrode exhibited a higher reversible capacity, especially at high rates, suggesting a faster ionic transfer and a lower kinetic barrier. This can be ascribed to the formation of stable Na-Al-O layer, which is conductive to Na^+ and facilitated the uniform and fast sodiation/desodiation during cycling [31,35,36]. Moreover, the Na storage behavior of the SC@Se and SC@Se-25Al_2O_3 electrodes was also investigated by cyclic voltammograms over a voltage range from 1.0 to 3.0 V (Fig. S16). As evidenced, only one redox pair of peaks was present between 1.0 V and 2.5 V in the first cycle for each electrode, indicating the full discharge product (Na_2Se) was formed from the chain-structure Se_n [16–19], and the peak shifted positively during the cathodic scan after the first cycle. The potential interval of the redox peaks in the 3rd cycle was calculated to be 0.44 V for the SC@Se-25Al_2O_3 electrode, which is much narrower than 0.476 V for the SC@Se electrode, reflecting the fast ionic transfer and improved electrochemical reaction kinetics owing to the Al_2O_3 modification.

Fig. 5c shows a long-term cycling test for SC@Se and SC@Se-25Al_2O_3 electrodes at 0.5 A g^{-1}, with which an initial discharge capacity of 760 and 707 mA h g^{-1} were achieved, respectively. Notably, a discharge capacity of 503.5 mAh g^{-1} was retained for the SC@Se-25Al_2O_3 electrode after 1000 cycles, whereas only 176 mAh g^{-1} after 660 cycles for the SC@Se electrode was found. Moreover, the SC@Se-25Al_2O_3 electrode even maintained 282 mAh g^{-1} after 500 cycles with a coulombic efficiency of 62.2% at a current density of 2 A g^{-1} (Fig. S17). To the best of our knowledge, this is the best cyclic stability performance for Na-Se batteries compared to the previous studies in the literature (Table S1).

In order to investigate the role of Al_2O_3 layer in protecting the electrodes, EIS on the fresh state and cycled states (1st, 20th and 40th) were carried out and shown in Fig. 5d and Fig. S18, respectively. In general, the Nyquist plot comprised a depressed semicircle in the high-to-middle frequencies corresponds to the charge-transfer resistance and

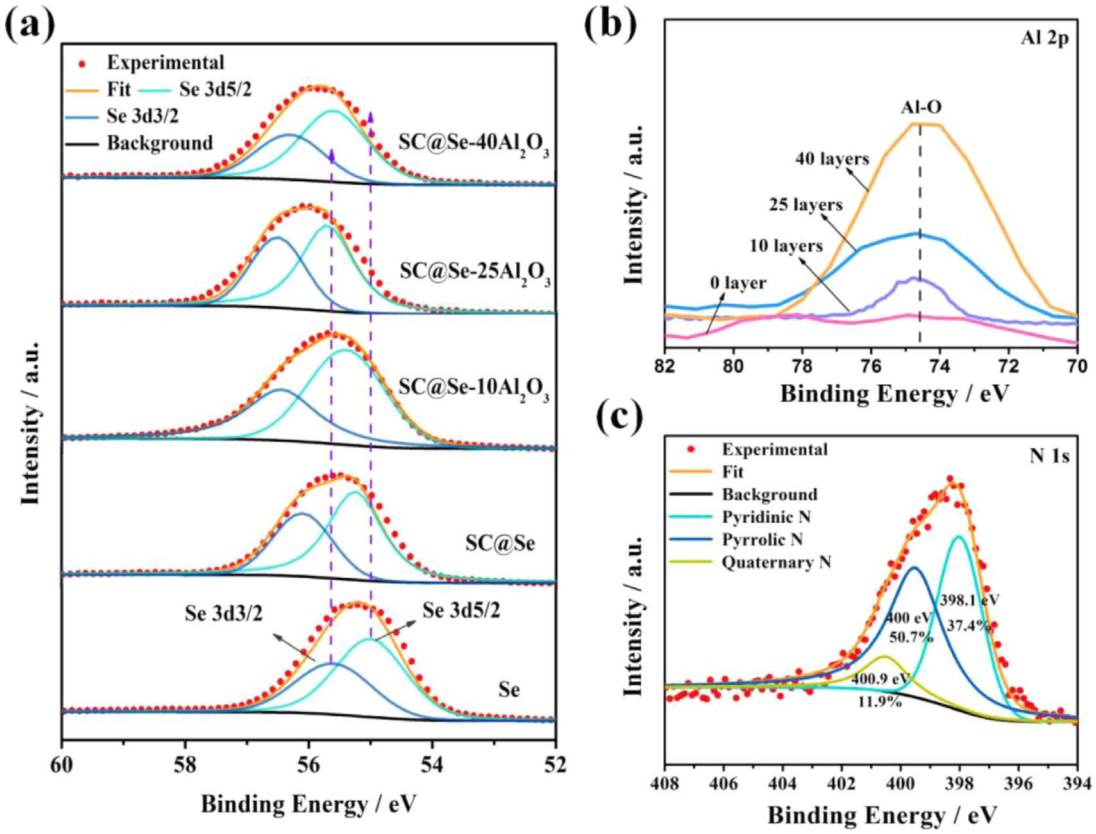

Fig. 4. XPS spectra of (a) Se 3d in pristine Se powder, SC@Se, and the SC@Se-xAl_2O_3 composites (x = 10, 25, and 40), (b) Al 2p in the SC@Se-xAl_2O_3 composites, and (c) N 1 s in PCNFs.

the straight sloping line at low frequency is related to the diffusion of sodium ions in the electrode [32,37–40]. The diameter of the semicircle represents the charge transfer resistance (R_{ct}), which is mainly generated at the interface between electrode and electrolyte and is expected to be electrolyte-Al_2O_3-Se in this work. Among them, the SC@Se-25Al_2O_3 electrode showed the smallest R_{ct} of 117 Ω before cycling and remained at 104 Ω, 214 Ω and 263 Ω after 1st (Fig. S18a), 20th (Fig. S18b) and 40th (Fig. S18c) cycling, respectively. However, the largest R_{ct} was seen for the SC@Se-40Al_2O_3 electrode (i.e., 402 Ω before cycling and changed to 337 Ω after 1st cycling, 542 Ω for 20th cycling and 655 Ω for 40th cycling, respectively), demonstrating that the thick layer blocked the ionic transfer. As shown in Fig. S18d, the bare SC@Se composite existed an obvious increment of R_{ct} from 1st to 40th cycle when compared with SC@Se-10Al_2O_3 and SC@Se-25Al_2O_3 electrodes. Thus, it can be concluded that an optimized ALD Al_2O_3 layer ensured the stable charge transfer and structural integrity of the electrodes, which led to good cycling performance and rate capability.

To scrutinize the improved cyclic stability due to the Al_2O_3 layer protection, the structural changes of the SC@Se-25Al_2O_3 electrode during charge/discharge processes were characterized by ex-situ FESEM measurement. It is clear that the structural integrity was retained except the growth of amorphous Se nanoparticles anchored on the surface of composite during the discharge process from 1.5 to 1.0 V (Fig. S19). However, the growth of Se nanoparticles resumed in the subsequent charge processes. Such the shape, size and structural integrity characteristics can be well maintained even after 300 cycles, with the uniform elemental distribution of Al, Na and Se elements along the entire nanofibers (Fig. S20), demonstrating a high structural stability enhanced by Al_2O_3 layer protection. For the SC@Se composites, the repeated volume variation during charge/discharge processes unavoidably caused the crack and pulverization of amorphous Se nanoparticles and conductive carbon matrix (Fig. S21), thus losing the conductive contact and leading to the capacity decay.

The mechanism for superior electrochemical performance of the SC@Se-25Al_2O_3 composites which benefit from the deposition of Al_2O_3 protective layer is proposed in Fig. 5e and f. First, the Al_2O_3 protective layer renders the structural integrity of electrode by suppressing the volume changes during charge/discharge processes. Second, the uniform and conformal Al_2O_3 layer serves as an artificial barrier to limit the dissolution of sodium polyselenides and mitigate the shuttle effects in electrolyte. Third, the Al_2O_3 protective layer also reduces the interfacial resistance, facilitating the charge transfer and Na^+ insertion, thus improving the rate capability (Fig. 5f).

4. Conclusions

In summary, Al_2O_3–coated (Se/porous N-doped carbon nanofibers) @Se composites (i.e., SC@Se-xAl_2O_3) were rationally designed and exploited as high-performance freestanding cathodes for Na-Se batteries. To improve the energy density of electrode, a facile strategy based on a two-step infiltration of Se in PCNFs was developed (i.e., yielding SC@Se), which enables the active mass loading of Se up to 70 wt%. More importantly, Al_2O_3 layer deposited on SC@Se by ALD was for the first time implemented for producing Se-based materials, conferring the long-term cycleability of Na-Se battery. Interestingly, the SC@Se-xAl_2O_3 composites with approximately 3-nm Al_2O_3 layer (x = 25) exhibited the best rate performance and cycling stability with a discharge capacity of 503.5 mAh g^{-1} after 1000 cycles at a current density of 0.5 A g^{-1}. This result can be ascribed to the synergy of N-doped 3D conductive carbon matrix and the Al_2O_3 layer protection, which resulted in good electrical conductivity, fast ionic/charge transfer, limited dissolution of sodium polyselenides into electrolyte, and suppressed volume expansion during charge/discharge processes. We envision that the strategy of constructing hierarchical structures (i.e., creating porous carbon nanofibers via electrospinning, decorating porous carbon nanofibers with Se, followed by coating Al_2O_3 layer for

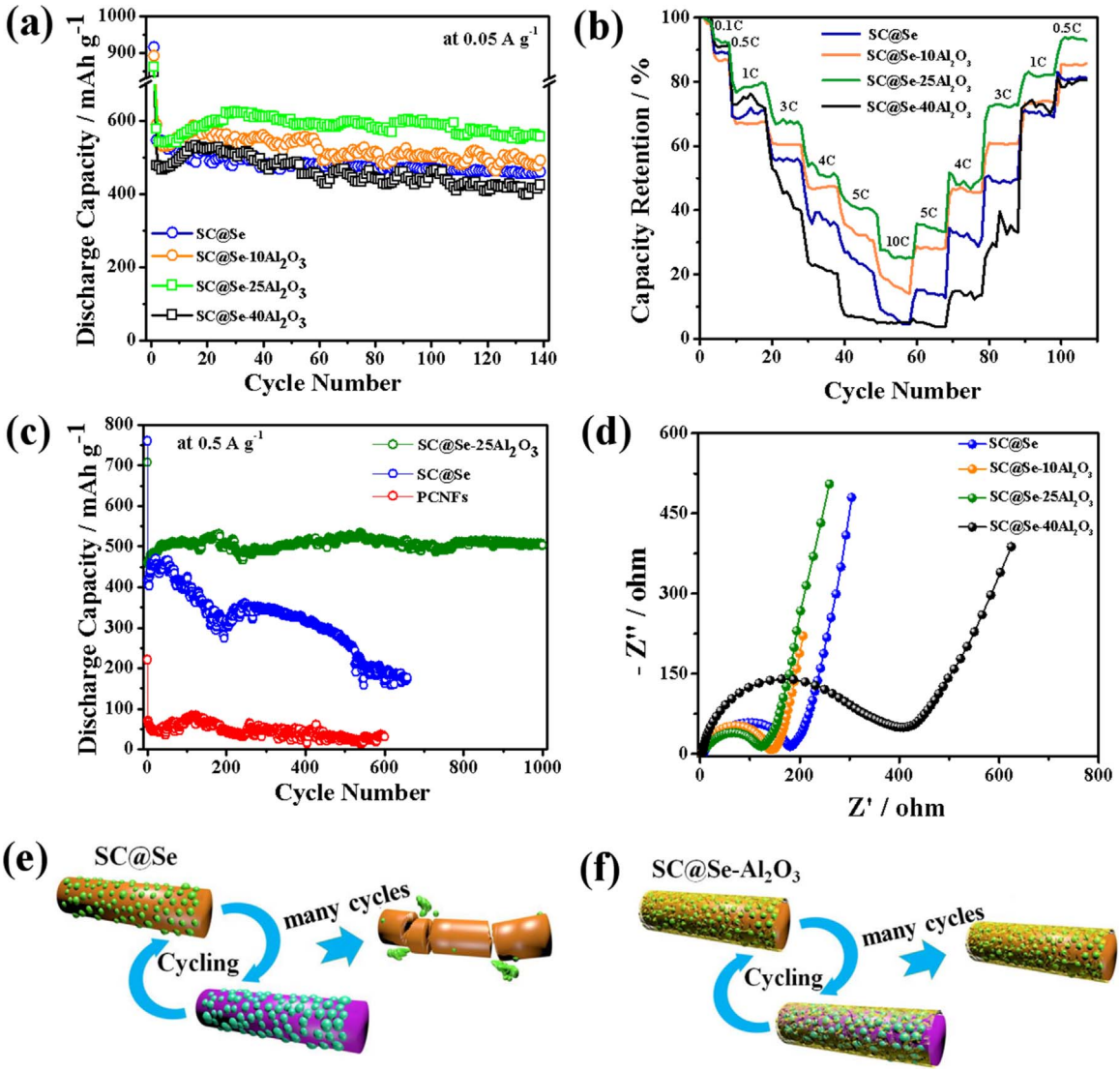

Fig. 5. (a) Cycle stability of SC@Se-xAl_2O_3 composites. (b) Comparison of the rate capability of SC@Se-xAl_2O_3 composites expressed as a percentage of the initial capacity at 0.1 C. (c) Comparison of long-term cycling stability of PCNFs, SC@Se, and SC@Se-25Al_2O_3 composites. (d) Nyquist plots of the SC@Se and SC@Se-xAl_2O_3 electrodes before cycling. (e) The proposed stabilizing effect of Al_2O_3 layer deposition on the SC@Se composites.

protection) can be easily extended to other electrode material systems to effectively impart high mass loading of material of interest and long cycle life of high-performance energy storage devices.

Acknowledgments

This work was supported by the National Natural Science Foundation of China (Nos. 51774203, 51374146, 51502177), the Natural Science Foundation of Guangdong (No. 2014A030310323), the Foundation of Guangdong Educational Committee (No. 2016KTSCX124), Shenzhen Science and Technology Project Program (Nos. ZDSYS201606061530079, KQJSCX20170327151152722, JCYJ20160422112012739), the National Natural Science Foundation of SZU (827-000039).

Appendix A. Supporting information

Supplementary data associated with this article can be found in the online version at http://dx.doi.org/10.1016/j.nanoen.2017.11.042.

References

[1] A. Vlad, N. Singh, C. Galande, P.M. Ajayan, Adv. Energy Mater. 5 (2015) 1402115.
[2] H.G. Wang, S. Yuan, D.L. Ma, X.B. Zhang, J.M. Yan, Energ. Environ. Sci. 8 (2015) 1660–1681.
[3] J. Peters, D. Buchholz, S. Passerini, M. Weil, Energ. Environ. Sci. 9 (2016) 1744–1751.
[4] H. Pan, Y.S. Hu, L. Chen, Energ. Environ. Sci. 6 (2013) 2338–2360.
[5] D. Kundu, E. Talaie, V. Duffort, L.F. Nazar, Angew. Chem. Int. Ed. 54 (2015) 3431–3448.
[6] W. Luo, F. Shen, C. Bommier, H. Zhu, X. Ji, L. Hu, Acc. Chem. Res. 49 (2016) 231–240.
[7] A. Abouimrane, D. Dambournet, K.W. Chapman, P.J. Chupas, W. Weng, K. Amine, J. Am. Chem. Soc. 134 (2012) 4505–4508.
[8] Q. Li, H. Liu, Z. Yao, J. Cheng, T. Li, Y. Li, C. Wolverton, J. Wu, V.P. Dravid, ACS Nano 10 (2016) 8788–8795.
[9] X. Wang, Z. Zhang, Y. Qu, G. Wang, Y. Lai, J. Li, J. Power Sources 287 (2015) 247–252.
[10] J.T. Lee, H. Kim, M. Oschatz, D.C. Lee, F. Wu, H.T. Lin, B. Zdyrko, W. Cho II, S. Kaskel, G. Yushin, Adv. Energy Mater. 5 (2015) 1400981.
[11] Z. Zhang, X. Yang, Z. Guo, Y. Qu, J. Li, Y. Lai, J. Power Sources 279 (2015) 88–93.
[12] J. Zhang, Y. Xu, L. Fan, Y. Zhu, J. Liang, Y. Qian, Nano Energy 13 (2015) 592–600.
[13] X. Li, J. Liang, K. Zhang, Z. Hou, W. Zhang, Y. Zhu, Y. Qian, Energ. Environ. Sci. 8 (2015) 3181–3186.
[14] C. Luo, Y. Xu, Y. Zhu, Y. Liu, S. Zheng, Y. Liu, A. Langrock, C. Wang, ACS Nano 7 (2013) 8003–8010.
[15] H. Wang, S. Li, Z. Chen, H.K. Liu, Z. Guo, RSC Adv. 4 (2014) 61673–61678.
[16] L. Zeng, X. Wei, J. Wang, Y. Jiang, W. Li, Y. Yu, J. Power Sources 281 (2015)

461–469.
[17] L. Zeng, W. Zeng, Y. Jiang, X. Wei, W. Li, C. Yang, Y. Zhu, Y. Yu, Adv. Energy Mater. 5 (2015) 1401377.
[18] S. Xin, L. Yu, Y. You, H.P. Cong, Y.X. Yin, X.L. Du, Y.G. Yu, Y. Cui, J.B. Goodenough, Nano Lett. 16 (2016) 4560–4568.
[19] X. Li, J. Liang, Z. Hou, W. Zhang, Y. Wang, Y. Zhu, Y. Qian, Adv. Funct. Mater. 25 (2015) 5229–5238.
[20] Z. Zhou, X. Gao, J. Yan, D. Song, Carbon 44 (2006) 939–947.
[21] K. Kaliyappan, J. Liu, A. Lushington, R. Li, X.L. Sun, ChemSusChem 8 (2015) 2537–2543.
[22] Y. Chen, S. Lu, J. Zhou, X. Wu, W. Qin, O. Ogoke, G. Wu, J. Mater. Chem. A 5 (2017) 102–112.
[23] F. Bingmei, W. Hui, Z.Q. Ying, S.Y. Xu, L. Min, L. Feng, J. Guo, J. Feng, H. Fang, 2D Materials 4 (2016) 015011.
[24] P. Zhou, Z. Zhang, H. Meng, Y. Lu, J. Cao, F. Cheng, Z. Tao, J. Chen, Nanoscale 8 (2016) 19263–19269.
[25] Y.S. Jung, P. Lu, A.S. Cavanagh, C. Ban, G.H. Kim, S.H. Lee, S.M. George, S.J. Harris, A.C. Dillon, Adv. Energy Mater. 3 (2013) 213–219.
[26] W. Luo, C.F. Lin, O. Zhao, M. Noked, Y. Zhang, G.W. Rubloff, L. Hu, Adv. Energy Mater. 7 (2017) 1601526.
[27] M. Létiche, E. Eustache, J. Freixas, A. Demortière, V. De Andrade, L. Morgenroth, P. Tilmant, F. Vaurette, D. Troadec, P. Roussel, T. Brousse, C. Lethien, Adv. Energy Mater. 7 (2017) 1601402.
[28] E.M. Lotfabad, P. Kalisvarrt, K. Cui, A. Kohandehghan, M. Kupsta, B. Olsen, D. Mitlin, Phys. Chem. Chem. Phys. 15 (2013) 13646–13657.
[29] A. Kohandehghan, P. Kalisvaart, K. Cui, M. Kupsta, E. Memarzadeh, D. Mitlin, J. Mater. Chem. A 1 (2013) 12850–12861.
[30] E.M. Lotfabad, P. Kalisvaart, A. Kohandehghan, K. Cui, M. Kupsta, B. Farbod, D. Mitlin, J. Mater. Chem. A 2 (2014) 2504–2516.
[31] X. Li, J. Liu, B. Wang, M.N. Banis, B. Xiao, R. Li, T.-K. Sham, X. Sun, RSC Adv. 4 (2014) 27126–27129.
[32] M. Yu, J. Ma, H. Song, A. Wang, F. Tian, Y. Wang, H. Qiu, R. Wang, Energ. Environ. Sci. 9 (2016) 1495–1503.
[33] G. Yu, L. Hu, N. Liu, H. Wang, M. Vosgueritchian, Y. Yang, Y. Cui, Z. Bao, Nano Lett. 11 (2011) 4438–4442.
[34] X. Han, Y. Gong, K. Fu, X. He, G.T. Hitz, J. Dai, A. Pearse, B. Liu, H. Wang, G. Rubloff, Y. Mo, V. Thangadurai, E.D. Wachsman, L. Hu, Nat. Mater. (2016), http://dx.doi.org/10.1038/nmat4821.
[35] X. Han, Y. Liu, Z. Jia, Y.C. Chen, J. Wan, N. Weadock, K.J. Gaskell, T. Li, L. Hu, Nano Lett. 14 (2014) 139–147.
[36] H. Kou, X. Li, H. Shan, L. Fan, B. Yan, D. Li, J. Mater. Chem. A 5 (2017) 17881–17888.
[37] D. Aurbach, M.D. Levi, E. Levi, H. Teller, B. Markovsky, G. Salitra, J. Electrochem. Soc. 145 (1998) 3024–3034.
[38] D. Aurbach, E. Zinigrad, Y. Cohen, H. Teller, Solid State Ion. 148 (2002) 405–416.
[39] D. Aurbach, J. Power Source 89 (2000) 206–218.
[40] J. Pokrzywinski, J.K. Kuem, R.E. Ruther, E.C. Self, M. Chi, H. Meyer III, K.C. Littrell, D. Aulakh, S. Marble, J. Ding, M. Wriedt, J. Nanda, D. Mitlin, J. Mater. Chem. A 5 (2017) 13511–13525.

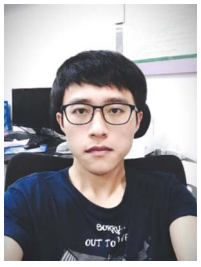

Dingtao Ma received the M.S. degree from Shenzhen University, China in 2016. He is currently a Ph.D. candidate at Macau University of Science and Technology, China. His research interests focus on high performance energy storage devices, and photothermal and photoelectric properties of two-dimensional materials.

Yongliang Li received the Ph.D. degree in Mechanical and Materials Engineering at University of Western Ontario, Canada in 2013. He is currently an associate researcher at Shenzhen University, China. His research interests focus on synthesis, characterization and application of nanomaterials for clean energy techniques, such as Li-ion batteries and Li-air batteries. He is an author and co-author of 60 papers in refereed journals.

Jingbo Yang received the B.S. degree in Nuclear Chemical and Engineering from Nanhua University, China in 2015. He is currently a Master student in Prof. Peixin Zhang's group at Shenzhen University, China. His research interests focus on the design and fabrication nanocarbons and transition mental compounds for Li-air batteries.

Hongwei Mi received the Ph.D. degree in Materials Science from China University of Geosciences in 2014. She worked in Shenzhen University as a lecturer from 2008. She was appointed as an associate researcher in 2017. Her research interests include the synthesis of nanomaterials and their related properties as well as their applications in batteries.

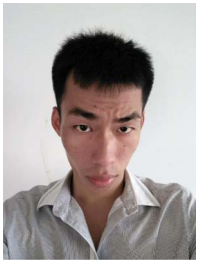

Shan Luo received the B.S. degree from Shandong Agricultural University, China in 2016. He is currently a Master student in the research group of Prof. Xiangzhong Ren at Shenzhen University, China. His scientific interests focus on theoretical calculation of electrochemical catalysis.

Libo Deng received the Ph.D. degree from University of Manchester, UK in 2011. He is currently an associate researcher at Shenzhen University, China. His research interests focus on carbon based energy storage and conversion materials.

Chaoyi Yan received the Ph.D. degree in 2011 from the Nanyang Technological University, Singapore. He worked in Peking University from 2015 to 2016 and then joined Shenzhen University as a full professor in Department of Applied Chemistry. His research interests include the synthesis, structural and property control of innovative nanomaterials for functional optoelectronic device applications, including but not limited to electrochemical energy storage devices, stretchable and wearable electronics, etc. He has authored more than 40 referred journal publications.

Peixin Zhang received the Ph.D. from Northeastern University, China in 1995. Currently, he is the Dean of College of Chemistry and Environmental Engineering at Shenzhen University, the Director of Shenzhen Key Laboratory of Environmental Chemistry and Ecological Remediation as well as the Director of Guangdong Flexible Wearable Energy and Device Engineering Technology Research Center. His research interests focus on design, synthesis and application of nanomaterials and related applications.

Zhiqun Lin received his Ph.D. in Polymer Science and Engineering from University of Massachusetts, Amherst in 2002. He is currently Professor of Materials Science and Engineering at the Georgia Institute of Technology. His research interests include perovskite solar cells, photocatalysis, hydrogen generation, batteries, semiconductor organic–inorganic nanocomposites, conjugated polymers, block copolymers, hierarchical structure formation and assembly, surface and interfacial properties, multifunctional nanocrystals, and Janus nanostructures.

Xiangzhong Ren received the Ph.D. degree from Sichuan University, China in 2007. He was appointed as a full professor at Shenzhen University, China in 2009. His research interests include the cathode and anode materials of lithium-ion batteries, nanocatalysts of lithium-air battery, nanocomposites, and their related properties.

Jianqing Li received the Ph.D. degree from Beijing University of Posts and Telecommunications, Beijing, China, in April 1999. From 2000 to 2002, he was a visiting professor of Information and Communications University, Daejeon, Korea. From 2002 to 2004, he was a research fellow of Nanyang Technological University, Singapore. He joined the Macau University of Science and Technology, Macau, in August 2004. Currently, he is a professor. His research interests are wireless networks, fiber sensors, energy storage and so on. He is a senior member of the Institute of Electrical and Electronics Engineers (IEEE).

Han Zhang received the Ph.D. degree from Nanyang Technological University, Singapore in 2011. He is a distinguished Professor at Shenzhen University, the director of Shenzhen Key Laboratory of Two-Dimensional Materials and Devices/Shenzhen Engineering Laboratory of Phosphorene. He is a winner of the National Thousand Talents Program for Distinguished Young Scholars, the National Science Fund for Excellent Young Scholars and the New Century Excellent Talent Award. His current research is focused on ultrafast and nonlinear photonics of 2D materials. He has published more than 100 papers (over 8500 total citations) and an H-index of 44.